Petroleum Science 20 (2023) 2253–2267

Contents lists available at ScienceDirect

Petroleum Science

journal homepage: www.keaipublishing.com/en/journals/petroleum-science

Original Paper

A two-phase type-curve method with multiscale fluid transport mechanisms in hydraulically fractured shale reservoirs

Feng-Yuan Zhang [a, b], Lin-Jun Zou [c], Zhen-Hua Rui [a, b, d, e, *], Hamid Emami-Meybodi [f], Luis F. Ayala [f], Zheng-Xin Zhang [a]

[a] College of Petroleum Engineering, China University of Petroleum (Beijing), Beijing, 102249, China
[b] National Key Laboratory of Petroleum Resources and Engineering, China University of Petroleum (Beijing), Beijing, 102249, China
[c] Oil and Gas Technology Research Institute, PetroChina Changqing Oilfield Company, Xi'an, 710000, Shaanxi, China
[d] College of Carbon Neutrality Future Technology, China University of Petroleum (Beijing), Beijing, 102249, China
[e] College of Petroleum, China University of Petroleum (Beijing) at Karamay, Karamay, 834000, Xinjiang, China
[f] College of Earth and Mineral Sciences, The Pennsylvania State University (University Park), State College, PA, 16802, USA

ARTICLE INFO

Article history:
Received 15 June 2022
Received in revised form
9 February 2023
Accepted 9 February 2023
Available online 11 February 2023

Edited by Yan-Hua Sun

Keywords:
Type curve
Two-phase flow
Flowback analysis
Fluid transport mechanisms
Shale reservoir

ABSTRACT

The quantitative understanding of hydraulic fracture (HF) properties guides accurate production forecasts and reserve estimation. Type curve is a powerful technique to characterize HF and reservoir properties from flowback and long-term production data. However, two-phase flow of water and hydrocarbon after an HF stimulation together with the complex transport mechanisms in shale nanopores exacerbate the nonlinearity of the transport equation, causing errors in type-curve analysis. Accordingly, we propose a new two-phase type-curve method to estimate HF properties, such as HF volume and permeability of fracture, through the analysis of flowback data of multi-fractured shale wells. The proposed type curve is based on a semianalytical solution that couples the two-phase flow from the matrix with the flow in HF by incorporating matrix influx, slippage effect, stress dependence, and the spatial variation of fluid properties in inorganic and organic pores. For the first time, multiple fluid transport mechanisms are considered into two-phase type-curve analysis for shale reservoirs. We analyze the flowback data from a multi-fractured horizontal well in a shale gas reservoir to verify the field application of the proposed method. The results show that the fracture properties calculated by the type-curve method are in good agreement with the long-time production data.

1. Introduction

1.1. Type-curve models

The evaluation of hydraulic fracturing (HF) performance and HF properties in shale reservoirs is one of the main challenges in the development of shale reservoirs (Guo et al., 2021; Sun et al., 2016). One way to economically estimate the HF properties is by analyzing early-time production data using theoretical approaches such as straight-line analysis and the type-curve method (Clarkson, 2013). The straight-line analysis approach is based on using diagnostic and specialty plots for identifying flow regimes and estimation of HF properties, respectively. Unlike the straight-line approach, the type-curve method relies on one plot with a set of curves, making its application simpler and faster. Type curves have been developed for both pressure transient analysis (Bourdet et al., 1989) and rate transient analysis under constant bottomhole pressure (BHP) conditions (Fetkovich, 1980) and variable bottomhole pressure/flowrate (Palacio and Blasingame, 1993). Type-curves are useful tools for estimating the reservoir, fracture, and wellbore properties.

The early type curves were mainly proposed for the unidirectional flow of vertical well, and there are only a few type curves that can analyze two-phase flow production data. Fetkovich (1980) obtained the constant BHP solution for the boundary-dominated flow (BDF) from a well centered in a reservoir with circular sealed boundary. Carter (1985) extended the applicability for Fetkovich type curves to gas reservoirs by proposing a modified type-curve that substitutes pseudopressure for pressure on the dimensionless decline rate axis. However, Fetkovich and Carter type curves are not applicable to variable BHP conditions. Considering

* Corresponding author. College of Petroleum Engineering, China University of Petroleum (Beijing), Beijing, 102249, China
E-mail address: ruizh@cup.edu.cn (Z.-H. Rui).

https://doi.org/10.1016/j.petsci.2023.02.004

more general variable pressure or rate conditions, Palacio and Blasingame (1993) used the Duhamel principle to define the reservoir material balance time and pseudotime, respectively. By modifying the dimensionless time, they proposed the Blasingame type-curve that shows a harmonic decline of the BDF solution at variable pressure/rate conditions. Using the dimensionless group introduced by Palacio and Blasingame (1993), Agarwal et al. (1999) generated Agarwal-Gardner type curves, distinguishing transient and BDF flow regimes. Wattenbarger et al. (1998) obtained the transient linear flow and linear BDF analytical solutions and generated type curves for rectangular drainage areas.

Recent studies have focused on developing type curves for multi-fractured horizontal wells (MFHWs). Nobakht et al. (2013) extended Wattenbarger et al. (1998) type curve to partially fractured reservoirs. The Blasingame type-curve was numerically extended to MFHWs by considering adsorption and diffusion for gas in a dual pore system (Lu et al., 2019). However, complex numerical models restrict the MFHWs application of type curves because of the nonuniqueness problem (Barzin and Mattar, 2017). For two-phase flow systems, Mohaghegh and Ertekin (1991) solved a one-dimensional governing equation and obtained a solution for gas and water flow in coalbed methane reservoirs. Then, they proposed the saturation/pressure-related dimensionless groups under an arithmetic average pressure. This results in having non-unique solutions under different reservoir properties. Thararoop et al. (2015) improved Mohaghegh and Ertekin (1991) type curve by considering the system of double pore and permeability. However, since dimensionless groups are evaluated approximately, the problem of non-uniqueness still exists. In addition, the existing two-phase type-curve is not suitable for shale reservoirs dominated by nanopores due to its incomplete factors and lack of consideration of oil-water and gas-water flow and the storage and transport mechanism of two-phase fluid for shale reservoirs.

1.2. Gas and water transport models

In shale reservoirs, gas stores in a free or sorbed state depending on the pore types, which can be organic and inorganic with clay minerals (Wang et al., 2017). Gas also dissolves in kerogen and other fluids. Many studies (Yang et al., 2016; Swami et al., 2013; Orozco and Aguilera, 2015) referred to Mehrotra and Svrcek (1982) for the dissolution and diffusion mechanism for gas in kerogen to study the dissolution mechanism of shale gas. Fick's law (Mi et al., 2014a, 2014b; Swami and Settari, 2012; Javadpour et al., 2013; Wu J. et al., 2015; Wei et al., 2016) can describe a gas diffusion in kerogen, but the determination of diffusion coefficient remains to be studied. Meanwhile, Darcy's law needs to be corrected before applying it to flow modeling in nanopores. Klinkenberg (1941) proposed to correct the gas slippage effect in the gas permeability measurement. With a study of the gradual decrease of reservoir core permeability, a high-order approximation equation is needed (Tang et al., 2005; Zhu et al., 2007; Gao et al., 2017) to correct permeability. Other scholars (Beskok et al., 1996; Javadpour, 2009; Sheng et al., 2014; Guo et al., 2015; Wang H. et al., 2015; Wang et al., 2016; Wu K.L. et al., 2015; Cao et al., 2022a, b) used theoretical methods to capture different transport and storage mechanisms, including Knudsen diffusion, molecular diffusion, surface diffusion, transitional flow, slippage effect, non-Darcy flow, stress sensitivity, and gas desorption.

For gas-water flow, Zhang et al. (2014) first studied the problem for fracturing fluid influx and flowback by using the high-density ratio Lattice Boltzmann method (LBM). Similarly, Suhrer et al. (2013) used high-density ratio LBM and digital core technology to simulate two-phase flow characteristics for gas-water. Most of the currently available models consider the influence of complex pores distribution characteristics on two-phase flow for gas-water, but cannot consider the scale effect of fluid flow in micro nanopores, such as adsorption layer on the hydrophilic wall and slip layer on the hydrophobic pore walls. Zhang et al. (2020) modified the boundary conditions for water flow in the LBM framework and established the LBM simulation method for water transport. Because the modified boundary conditions can only describe whether boundary slip occurs for water, but cannot effectively identify and describe boundary layer properties, such as near-wall fluid density and viscosity. Thus, based on the consideration of fluid-fluid and fluid-wall forces, the two-phase interface characteristics for gas-liquid and solid-liquid boundary layer characteristics are successfully identified (Zhang et al., 2021). Therefore, on the basis of existing simulation methods, the interaction between fluid and near-wall is coupled to effectively identify and quantify the properties of the near-wall fluid (boundary layer) and include two-phase flow for gas-water simulation for shale complex pore network.

1.3. Oil and water transport models

Javadpour et al. (2015) considered a slippage flow for water on the pore surface of shale by modifying Darcy's law, proposed a flow model for Newtonian fluids in capillaries of different shapes based on computational fluid mechanics, and measured slippage coefficients for different shale samples using atomic force microscopy (Li et al., 2016). Through laboratory experiments, Wu et al. (2017) studied the adsorption and distribution for water in shale pores. By introducing the concept of effective slippage length, the spatial distribution of water viscosity at the continuous area and surface area in the pore is considered (Zhang et al., 2018). A stochastic apparent permeability model was developed to represent water flow in the mixed wetted material (Zeng et al., 2020). Wang S. et al. (2015) proposed an apparent permeability model for water using fractal theory. The above-mentioned studies are mainly applied to the leak-off of fracturing fluid into a shale matrix since it only focuses on a storage and transport mechanism for water.

Zhang et al. (2017) studied the adsorption and migration of oil in shale organic or inorganic pores through molecular dynamics simulation. Cui et al. (2017) proposed an apparent permeability model transport for shale, taking into account slippage length, pore aperture, and oil properties in pores with different wettability. Cui (2019) proposed a liquid permeability model taking into account oil films on organic pore walls and then improved the model to consider wettability alteration, pore shrinkage, and viscosity changes caused by asphaltene precipitation. Wang et al. (2019) suggested that the elliptic capillary model represents the real shape of nanopores for shale and studied the effect of different nanopore curvatures on the oil flow. Zhang et al. (2019) used LBM to integrate a single capillary model into a complex pore network and obtained an apparent permeability model suitable in shale reservoirs. In addition, they discussed the influence of organic matter content, and distribution on fluid transport. The above-mentioned studies focus only on single-phase oil transport in shales.

There are few studies on nano-scale two-phase flow (Fan et al., 2020), and the difficulties are reflected in the measurement of nano-scale transport and the mixed wettability of shale reservoirs (Abbasi et al., 2012). Due to the influx of fracturing fluid to fracture, the two-phase flow of oil and water is expected during the early flowback stage, and the storage and transport mechanisms for the two-phase flow need to be considered in the flowback modeling.

We propose a type-curve method for the estimation of HF properties using two-phase flow production data. A semianalytical model is developed by considering hydrocarbon-water two-phase storage and transport mechanisms. The model is then used to

generate a type curve for the estimation of fracture properties and the evaluation of HF performance. The type curve is a function of dimensionless parameters that hold HF properties. Unlike the existing type-curve methods, the proposed method is not subject to non-unique solutions and considers shale reservoirs' key storage and transport mechanisms. The field application of the proposed method is verified using flowback and long-term production data from an MFHW in a shale gas reservoir.

2. Model and theory

We first describe the conceptual model of two-phase flow and introduce main assumptions. Then, we present the mathematical model for the fracture and matrix system. Next, we explain procedures for including storage and transport mechanisms. Finally, the type-curve method is described along with the workflow to estimate HF and matrix properties.

2.1. Conceptual model

Fig. 1 depicts the conceptual model used in this study. After hydraulic fracturing, fractures are mainly filled with fracturing fluid (water phase), and the rest is a hydrocarbon (oil or gas). During the early flowback, water is mainly produced. The majority of the produced water comes from fractures, with a small amount coming from the matrix. Over time, water production reduces, and hydrocarbon production increases as hydrocarbon influx from matrix to fracture increases.

On the surface of organic nanopores, hydrocarbon molecules can form adsorption layers with the adsorbed viscosity ($\mu_{h,om}$) and density ($\rho_{h,om}$) being more than the bulk hydrocarbon values, and their slip length ($\lambda_{h,om}$) is less than that of bulk hydrocarbon. In inorganic nanopores, however, hydrocarbon fluids mainly occupy the bulk region (free pore space) and the water phase is distributed near the wall region. Water adsorbs on the inorganic pore surfaces

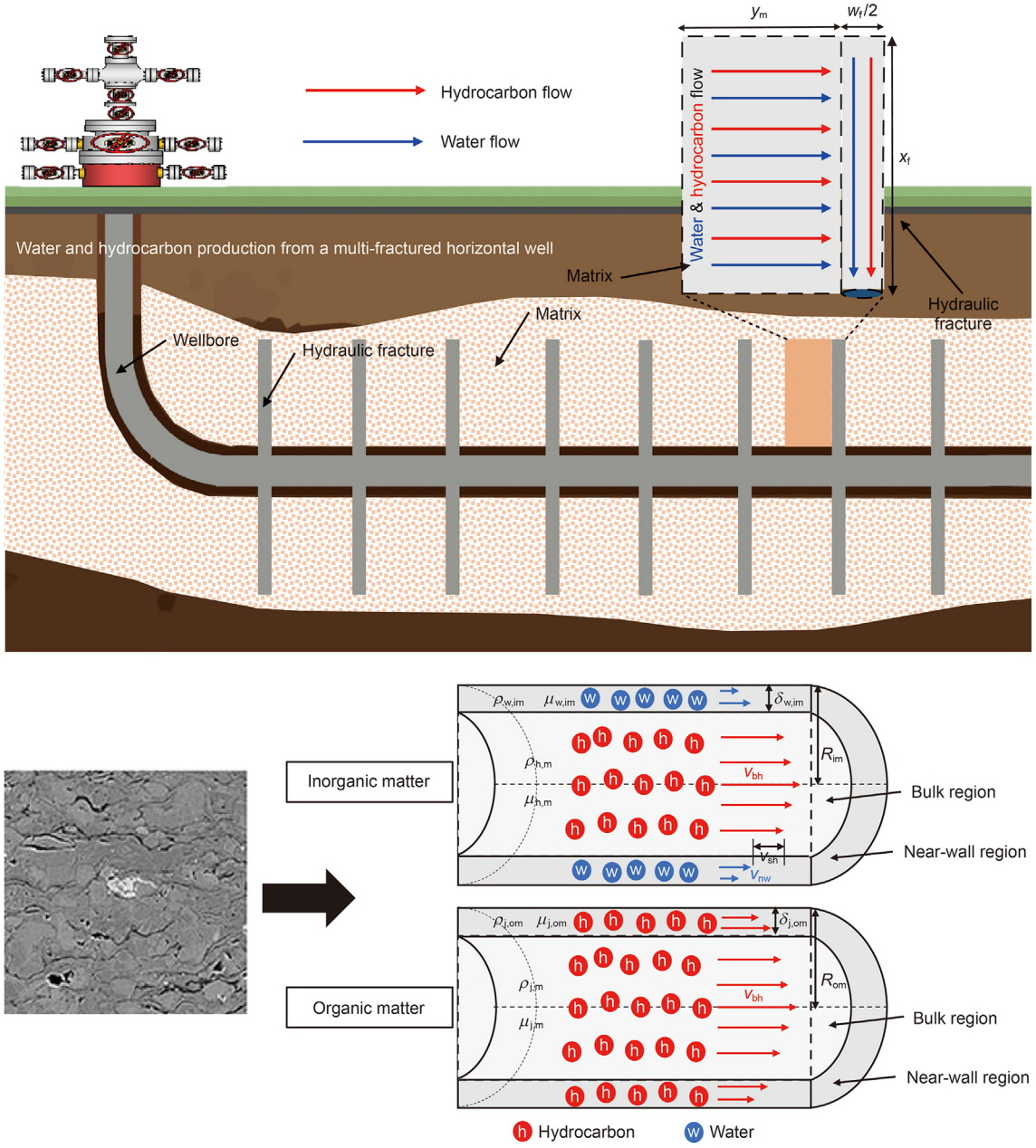

Fig. 1. Conceptual model of two-phase flowback flow in a shale reservoir.

and creates an adsorption layer. The viscosity ($\mu_{w,im}$) and density ($\rho_{w,im}$) of adsorbed water are greater than the bulk water due to the strong interaction of water molecules with the pore walls. This extra flow resistance generally leads to small slip lengths ($\lambda_{w,im}$) of the adsorbed layer or even no-slip boundary conditions. Meanwhile, the hydrocarbon viscosity ($\mu_{h,im}$) and density ($\rho_{h,im}$) decrease and the slip length ($\lambda_{h,im}$) increases at the interface between hydrocarbon and water in the bulk and near-wall regions because of the weak interaction between hydrocarbon and water. To fill in the research gap on the two-phase storage and transport model for shale nanopores, we first establish the expression of organic or inorganic nanopores apparent permeability and then integrate it with the volume fraction of organic material.

The main assumptions used in the conceptual model are as follows:

- During the flowback, two-phase flow of hydrocarbon and water exists in both fracture and matrix.
- The fracture and matrix are homogeneous and isotropic, which neglects the gradient of pressure and saturation along the fracture. The fluid flow in the fracture obeys Darcy's law, and the effects of gravity and capillary are ignored.
- The fluid contribution outside the fracture tip is ignored, and the hydraulic fracture fully penetrates through the formation.
- Inorganic and organic pores are assumed to be parallel with no communication between them (Sun et al., 2017; Wang et al., 2018; Li et al., 2020).
- Under the same pore pressure, the matrix has similar stress dependence for organic and inorganic matters. The permeability and porosity of both fracture and matrix exponentially decrease with pressure drop (Yilmaz et al., 1994).
- Fracture, matrix, oil, and water are slightly compressible with constant but different compressibility coefficients. Real gas law is valid for the gas. Fluid properties are pressure-dependent.
- Due to the hydrophilicity of the inorganic matter, the fracturing fluid mainly invades into the inorganic nanopores. Water molecules in inorganic pores are mainly distributed in the near-wall region (Tao et al., 2018; Shen et al., 2019). The hydrophilicity of the near-wall region makes the slippage effect at the liquid-solid interface negligible. The slippage effect between hydrocarbon and water layers in the nanopore is ignored.
- Due to the hydrophobicity of organic matter, fracturing fluid intruded into organic pores during stimulated reservoir can be ignored. Organic nanopores are assumed to contain single-phase hydrocarbon only.
- The reservoir remains undersaturated during the flowback period. For gas reservoirs, the condensate at wellbore and formation is ignored. For oil reservoirs, gas production from oil is ignored.
- The organic nanopores storage and transport of oil follow the model proposed by Zhang and Emami-Meybodi (2021b) for shale oil reservoir, which includes slippage and uneven distribution of fluid properties in the near-wall or bulk region.
- The storage and transport of gas in organic pores follow the model proposed by Zhang and Emami-Meybodi (2021a), which includes slippage, Knudsen diffusion, surface diffusion, and Langmuir monolayer adsorption.

2.2. Analytical model and type curve

2.2.1. Fracture solution

First, we derived the semianalytical model for the constant rate condition. Then, we expanded it to the variable rate/pressure conditions using the Duhamel principle (Özisik and Ã–zisik, 1993). Finally, we transformed the model into a type-curve form and evaluated fracture properties.

Based on the flowback studies for the gas (Zhang and Emami-Meybodi, 2021a) and oil reservoirs (Zhang and Emami-Meybodi, 2021b), we adopted the following governing equation and initial/boundary conditions for fluid flow in fracture. All the parameters related to fluid in this study (such as fluid viscosity, compressibility, fluid influx, etc.) should contain an implicit subscript j, which represents either water (j = w), oil (j = o), or gas (j = g) phase. However, to improve the readability of this study, we omitted the subscript j for each phase on all fluid-dependent parameters since the hydrocarbon-phase and water-phase equations have the same form in expression.

$$\frac{\partial}{\partial x}\left(\frac{k_{r,f}k_f}{\mu_f B_f}\frac{\partial p_f}{\partial x}\right)=\frac{157.98\phi_f C_{e,f}}{B_f}\frac{\partial p_f}{\partial t}, \tag{1}$$

$$p_f(x,0)=p_{fi},\quad w_f h\left(\frac{k_{r,f}k_f}{\mu_f B_f}\frac{\partial p_f}{\partial x}\right)\Big|_{x=0}=259.133q,\frac{\partial p_f}{\partial x}\Big|_{x=x_f}=0, \tag{2}$$

$$C_{e,f}=S_f\left(C+C_f\right)+\frac{dS_f}{dp_f}-\frac{q_s B_f}{2h\,x_f w_f \phi_f}\frac{\partial t}{\partial p_f}, \tag{3}$$

where x is the distance in fracture, ft; t is the time, day; $k_f=k_{fi}\exp(-\gamma_f(p_{fi}-p_f))$ is the fracture permeability, mD; $k_{r,f}$ is the fracture relative permeability; k_{fi} is the fracture permeability at the initial condition, mD; γ_f is the fracture permeability modulus, psi^{-1}; p_{fi} is the initial fracture pressure, psi; p_f is the pore pressure in fracture, psi; μ_f is the fluid viscosity in the fracture, cP; B_f is the formation-volume-factor for each phase of fluid in fracture, ft^3/STB; $\phi_f=\phi_{fi}\exp(-C_f(p_{fi}-p_f))$ is the fracture porosity; ϕ_{fi} is the fracture porosity at the initial pressure; x_f is the fracture half-length, ft; w_f is the fracture width, ft; h is the fracture height, ft; q is the flowrate for each phase of fluid at the surface conditions, STB/day; S_f is the fluid saturation in the fracture; C_f is the fracture compressibility, psi^{-1}; $C_{e,f}$ is the fracture effective compressibility, psi^{-1}; C is the compressibility for each phase of fluid in the fracture, psi^{-1}; q_s is the fluid influx from matrix to fracture at the surface conditions, STB/day.

The pressure-dependent rock and fluid properties in Eqs. (1) and (2) make the governing equation highly nonlinear. By introducing fracture pseudopressure and pseudotime shown in Table 1, the governing equation can be linearized:

$$\frac{\partial^2 m_f(p_f)}{\partial x^2}=\frac{157.98}{\eta_f}\frac{\partial m_f(p_f)}{\partial t_{p,f}}, \tag{4}$$

$$m_f\left[p_f(x,0)\right]=m_f(p_{fi}),\quad \frac{\partial m_f(p_f)}{\partial x}\Big|_{x=0}=\frac{259.133q\mu_{fi}B_{fi}}{2w_f h k_{fi}},\frac{\partial m_f(p_f)}{\partial x}\Big|_{x=x_f}=0, \tag{5}$$

Table 1
Definitions of the fracture and matrix pseudo variates and dimensionless variates.

Variates		Pressure	Time	Distance
Pseudo variates	Fracture	$m_f(p) = \left(\frac{\mu_f B_f}{k_f}\right)_i \int_{p_b}^{p} \frac{k_f(p)\, k_{r,f}(S_f)}{\mu_f(p) B_f(p)} dp$	$t_{p,f} = \left(\frac{\phi_f \mu_f C_{e,f}}{k_f}\right)_i \int_0^t \frac{k_f(\bar{p}_f) k_{r,f}(\bar{S}_f)}{\phi_f(\bar{p}_f)\mu_f(\bar{p}_f) C_{e,f}(\bar{p}_f)} dt$	–
	Matrix	$m_m(p) = \left(\frac{\mu_m B_m}{k_m}\right)_i \int_{p_b}^{p} \frac{k_{j,m}(p, S_m)\, k_{r,m}(S_m)}{\mu_m(p) B_m(p)} dp$	$t_{p,m} = \left(\frac{\phi_m \mu_m C_{e,m}}{k_m}\right)_i \int_0^t \frac{k_{j,m}(\bar{p}_m, \bar{S}_{j,m}) k_{r,m}(\bar{S}_m)}{\phi_m(\bar{p}_m)\mu_m(\bar{p}_m) C_{e,m}(\bar{p}_m)} dt$	–
Dimensionless variates	In terms of w_f	$p_D = \frac{k_{fi} h [m_f(p_{fi}) - m_f(p_f)]}{\alpha_j q \mu_{fi} B_{fi}}$	$t_{Dw} = \frac{\beta \eta_f t_{p,f}}{w_f^2/4}$	$x_{Dw} = \frac{2x}{w_f}$
	In terms of x_f	$p_D = \frac{k_{fi} h [m_f(p_{fi}) - m_f(p_f)]}{\alpha_j q \mu_{fi} B_{fi}}$	$t_{Dx} = \frac{\beta \eta_f t_{p,f}}{x_f^2}$	$x_D = \frac{x}{x_f}$

While j = w and o: $\alpha_j = 25.149$. While j = g: $\alpha_j = 25149$. $\beta = 0.00633$.

where $\eta_f = \left(\frac{k_f}{\phi_f \mu_f C_{e,f}}\right)_i$, $t_{p,f}$ and $m_f(p)$ are the fracture pseudotime (day) and pseudopressure (psi) for each phase of fluid, respectively.

We first used w_f as the characteristic length to define the dimensionless parameters (see Table 1) and solve Eqs. (4) and (5). The governing equation with the initial and boundary conditions in the dimensionless form are given by:

$$\frac{\partial^2 p_D}{\partial x_{Dw}^2} = \frac{\partial p_D}{\partial t_{Dw}}, \tag{6}$$

$$p_D[p_f(x,0)] = 0, \quad \left.\frac{\partial p_D}{\partial x_{Dw}}\right|_{x_{Dw}=0} = \frac{1}{4}, \quad \left.\frac{\partial p_D}{\partial x_{Dw}}\right|_{x_{Dw}=x_{Df}} = 0, \tag{7}$$

where $x_{Df} = \frac{2x_f}{w_f}$ is the dimensionless distance; p_D is the fracture dimensionless pseudopressure; t_{Dw} is the fracture dimensionless pseudotime; and x_{Dw} is the dimensionless distance.

Solving Eqs. (6) and (7) (Miller, 1962) gives:

$$p_D = \frac{\pi}{2} x_{Df} \left[\frac{1}{3} - \frac{x_{Dw}}{x_{Df}} + \frac{1}{2}\frac{x_{Dw}^2}{x_{Df}^2} + \frac{t_{Dw}}{x_{Df}^2} - 2\Sigma_{n=1}^{\infty} \frac{1}{(n\pi)^2} \cos\left(\frac{n\pi x_{Dw}}{x_{Df}}\right) \exp\left(-\frac{(n\pi)^2 t_{Dw}}{x_{Df}^2}\right)\right], \tag{8}$$

and substituting $x_{Dw} = 0$ into Eq. (8) gives

$$p_{wD} = \frac{\pi}{2} x_{Df} \left[\frac{1}{3} + \frac{t_{Dw}}{x_{Df}^2} - 2\Sigma_{n=1}^{\infty} \frac{1}{(n\pi)^2} \exp\left(-\frac{(n\pi)^2 t_{Dw}}{x_{Df}^2}\right)\right], \tag{9}$$

where p_{wD} is the dimensionless pseudopressure for p_{wf}.

The analytical solution given by Eq. (9) is based on three dimensionless parameters p_{wD}, x_{Df}, and t_{Dw}. The efficient way to solve the solution is by generating p_{wD} vs. t_{Dw} curves in a log-log plot (Wattenbarger et al., 1998). However, to simplify the procedure of curve-matching, we defined a new set of dimensionless variables by choosing x_f as the characteristic length (see Table 1). Accordingly, Eq. (9) can be written as:

$$\left(\frac{w_f}{2x_f}\right) p_{wD} = \frac{\pi}{2}\left[\frac{1}{3} + t_{Dx} - 2\Sigma_{n=1}^{\infty} \frac{1}{(n\pi)^2} \exp\left(-(n\pi)^2 t_{Dx}\right)\right], \tag{10}$$

where t_{Dx} is the dimensionless pseudotime (in terms of x_f) for the fracture. Compared with Eq. (9), Eq. (10) has one less dimensionless parameter and is only based on $(w_f/2x_f)p_{wD}$ and t_{Dx}. This further simplifies the use of type-curve and reduces the matching process erorr.

Fig. 2a depicts the generated type-curve using Eq. (10), where the x-axis represents t_{Dx} and the y-axis represents $(2x_f/w_f)/p_{wD}$, $(w_f/2x_f)p_{wD}'$, and $(2x_f/w_f)/\mathrm{dln}p_{wD}'$. $1/p_{wD}$ was used for the y-axis instead of p_{wD} to get a monotonically decreasing type curve. The type curve (solid blue curve) can be seen as two straight lines: the early-time straight-line with a negative half-slope corresponding to the infinite acting linear flow (IALF) in the fracture, and the late-time straight-line with the negative unit slope corresponding to the BDF in the fracture (Zhang and Emami-Meybodi, 2021a).

Fig. 2 also shows two additional derivative curves that can be used for the flow regime identification (Agarwal et al., 1999), including the derivative of p_{wD} with respect to t_{Dw} (i.e. p_{wD}' or dp_{wD}/dt_{Dw}) and the inverse log-time derivative of p_{wD} (i.e. $1/\mathrm{dln}p_{wD}'$ or $1/(dp_{wD}/\mathrm{dln}t_{Dw})$). p_{wD}' curve behaves similarly to $1/p_{wD}$ curve with a difference in the time at which IALF changes to BDF, which is earlier in the p_{wD}' curve than the $1/p_{wD}$ curve. Unlike the $1/p_{wD}$ and $1/\mathrm{dln}p_{wD}'$ curves, the p_{wD}' curve presents a straight line with a zero slope for fracture BDF.

As shown in Fig. 2a, a single curve represents the proposed type curve, and the analysis does not rely on a family of curves for the different fracture dimensions. In addition, both $(2x_f/w_f)/p_{wD}$ and $(2x_f/w_f)/\mathrm{dln}p_{wD}'$ curves follow the negative half-slope straight-lines at early times and then the slopes change to the negative one during the late time. During fracture BDF, both curves have the characteristics of converging to harmonic decline consistent with Blasingame type curves (Palacio and Blasingame, 1993). As mentioned earlier, $(2x_f/w_f)/p_{wD}$ curve shows an earlier transition from IALF to BDF as compared with $(w_f/2x_f)p_{wD}'$ and $(2x_f/w_f)/\mathrm{dln}p_{wD}'$ curve. Accordingly, the derivative curves provide the time when the fracture flow becomes BDF more accurately.

We used the superposition pseudotime t_{sp} and dimensionless superposition pseudotime t_D to extend the analytical solution to the variable rate/pressure conditions (Zhang and Emami-Meybodi, 2022):

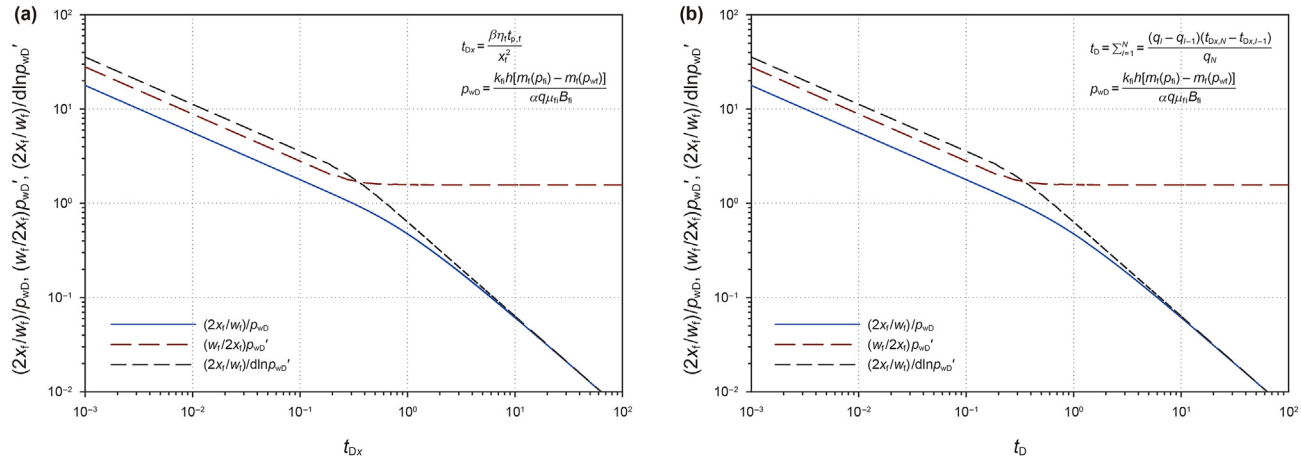

Fig. 2. Generated type curves in terms of x_f for the constant (**a**) and variable (**b**) rate conditions (Zhang and Emami-Meybodi, 2022).

$$t_{sp}=\Sigma_{l=1}^{N}\frac{(q_l-q_{l-1})\left(t_{p,f,N}-t_{p,f,l-1}\right)}{q_N}, \tag{11}$$

$$t_D=\frac{\beta\eta_f t_{sp}}{x_f^2}=\Sigma_{l=1}^{N}\frac{(q_l-q_{l-1})\left(t_{Dx,N}-t_{Dx,l-1}\right)}{q_N}. \tag{12}$$

Boundary conditions given by Eq. (2) can be extended to the variable rate conditions using Eqs. (11) and (12). In addition, Eq. (10) can be applied to the variable rate/pressure conditions using the Duhamel's principle (Özisik and Ã–zisik, 1993):

$$\left(\frac{w_f}{2x_f}\right)p_{wD}=\frac{\pi}{2}\left[\frac{1}{3}+t_D-2\Sigma_{l=1}^{N}\frac{(q_l-q_{l-1})}{q_N}\Sigma_{n=1}^{\infty}\frac{1}{(n\pi)^2}\exp\left(-(n\pi)^2\left(t_{Dx,N}-t_{Dx,l-1}\right)\right)\right]. \tag{13}$$

Eq. (13) presents an exact solution for the variable rate/pressure conditions. However, it is challenging to generate a type curve directly using Eq. (13). Hence, we introduce the following relationship to simplify the complicated exact solution.

$$\Sigma_{l=1}^{N}\frac{(q_l-q_{l-1})}{q_N}\Sigma_{n=1}^{\infty}\frac{\exp\left(-(n\pi)^2\left(t_{Dx,N}-t_{Dx,l-1}\right)\right)}{(n\pi)^2}\approx\Sigma_{n=1}^{\infty}\frac{\exp\left(-(n\pi)^2\Sigma_{l=1}^{N}\frac{(q_l-q_{l-1})\left(t_{Dx,N}-t_{Dx,l-1}\right)}{q_N}\right)}{(n\pi)^2}. \tag{14}$$

By substituting Eq. (14) into Eq. (13), the exact solution for variable rate condition in Eq. (13) can be approximated in the form of constant rate solution with the help of dimensionless superposition pseudotime t_D:

$$\left(\frac{w_f}{2x_f}\right)p_{wD}=\frac{\pi}{2}\left[\frac{1}{3}+t_D-2\Sigma_{n=1}^{\infty}\frac{1}{(n\pi)^2}\exp\left(-(n\pi)^2t_D\right)\right]. \tag{15}$$

During fracture BDF period, the summation terms in Eqs. (14) and (15) can be neglected because as the time increases the exponential term becomes very small and the summation term approaches zero (Wattenbarger et al., 1998). This approximation is still valid when flowrate changes are negligible for the early-time production. Therefore, we used Eq. (15) as the type curve solution for variable rate/pressure conditions, which can be plotted in Fig. 2b.

2.2.2. Matrix solution

The governing equation and initial/boundary conditions for the matrix are as follows (Zhang and Emami-Meybodi, 2022):

$$\frac{\partial}{\partial y}\left(\frac{k_{r,m}k_{j,m}}{\mu_m B_m}\frac{\partial p_m}{\partial y}\right)=\frac{157.98\phi_m C_{e,m}}{B_m}\frac{\partial p_m}{\partial t}, \tag{16}$$

$$p_m(y,0)=p_{mi},\quad p_m(0,t)=\overline{p}_f,\quad \left.\frac{\partial p_m}{\partial y}\right|_{y=y_m}=0, \tag{17}$$

$$C_{e,m}=S_m(C+C_m)+\frac{dS_m}{dp_m}, \tag{18}$$

where y is the distance in the matrix, ft; $k_{r,m}$ is the matrix relative permeability; $k_{j,m}$ is the matrix apparent permeability for each phase which will be elaborated in the next section; γ_m is the permeability modulus for the matrix, psi^{-1}; $\phi_m=\phi_{mi}\exp[-C_m(p_{mi}-p_m)]$ is the pressure-dependent matrix porosity; C_m is the matrix compressibility, psi^{-1}; k_{mi} and ϕ_{mi} are the matrix permeability (mD) and porosity at the initial matrix pressure p_{mi}, respectively; p_m is the matrix pressure, psi; μ_m is the viscosity of fluid in the matrix for each phase, cP; B_m is the formation-volume-factor of fluid in the matrix for each phase, ft^3/STB; $\overline{p}_f$ is the average fracture pressure, psi; y_m is the fractures half-spacing, ft; $C_{e,m}$ is the matrix effective compressibility, psi^{-1}; S_m is the fluid saturation in the matrix; and C_m is the compressibility of fluid in the matrix for each phase, psi^{-1}.

Using the matrix pseudopressure $m_m(p)$ and pseudotime $t_{p,m}$ (see Table 1), we linearized and solved Eqs. (16) and (17) (Özisik and Ã–zisik, 1993):

$$q_s=\frac{[m_m(p_{mi})-m_m(p_b)]\,x_f h\,k_{j,mi}}{\delta_j(\mu B)_{mi}y_m}\Sigma_{l=0}^{N-1}\left[\Sigma_{n=1}^{\infty}\exp\left(-\beta_n^2\frac{\eta_m\left(t_{p,m}-t_{p,m,l}\right)}{y_m^2}\right)\Delta\zeta(t)_l\right], \tag{19}$$

$$q_{s,IALF}=\frac{[m_m(p_{mi})-m_m(p_b)]\,x_f\,h\,k_{j,mi}}{\varepsilon_j(\mu B)_{mi}\sqrt{\eta_m}}\Sigma_{l=0}^{N-1}\frac{\Delta\zeta(t)_l}{\sqrt{\left(t_{p,m}-t_{p,m,l}\right)}}, \tag{20}$$

$$J_{o,om}=3.62\times10^8\frac{\rho_{o,m}\pi(R_{om}-\delta_{j,om})^2}{8}\left[\frac{4R_{om}\delta_{o,om}-2\delta_{o,om}^2+4\lambda_{o,om}R_{om}}{\mu_{o,om}}+\frac{(R_{om}-\delta_{o,om})^2}{\mu_{o,m}}\right]\frac{\partial p_m}{\partial y}+$$
$$3.62\times10^8\frac{\rho_{o,om}\pi\left(2R_{om}\delta_{o,om}-\delta_{o,om}^2\right)}{8\mu_{o,om}}\left(2R_{om}\delta_{o,om}-\delta_{o,om}^2+4\lambda_{o,om}R_{om}\right)\frac{\partial p_m}{\partial y}, \tag{25}$$

$$Q_s=\int_0^t q_s dt,\quad \eta_m=\left(\frac{k_{j,m}}{\phi_m\mu C_{e,m}}\right)_i, \tag{21}$$

$$\Delta\zeta(t)_l=\zeta(t)_{l+}-\zeta(t)_{l-}, \tag{22}$$

$$\zeta(t)=\frac{m_m(p_{mi})-m_m\left(\overline{p}_f(t)\right)}{m_m(p_{mi})-m_m(p_b)}, \tag{23}$$

where $\beta_n=(2n-1)\pi/2$; Q_s is the cumulative fluid influx from matrix to fracture for each phase, STB; p_b is the base pressure, psi; and δ_j and ε_j are the unit conversion factors: for j = w or o, $\delta_j=19.757$ and $\varepsilon_j=5.575$ (Zhang and Emami-Meybodi, 2021b) and for j = g, $\delta_j=19757$ and $\varepsilon_j=5575$ (Zhang and Emami-Meybodi, 2021a). Eq. (19) is the exact analytical solution for the matrix during IALF and BDF regimes, while Eq. (20) represents the short-term approximation valid only for IALF.

2.3. Two-phase storage and transport mechanisms

2.3.1. Organic pores

Due to the hydrophobicity of organic matter, only single-phase gas or oil exists in the organic pores. The total mass flux ($J_{g,om}$) of gas in organic pores can be obtained by considering multiple gas storage and transport mechanisms, including adsorption, diffusion, and slip flow (Zhang and Emami-Meybodi, 2021a):

$$J_{g,om}=\left(\frac{1}{1+K_{n,om}}\right)J_{sl,om}+\left(\frac{1}{1+1/K_{n,om}}\right)J_{k,om}+J_{sf,om}, \tag{24}$$

where $K_{n,om}$ is the Knudsen coefficients of organic matter; $J_{sl,om}$ is the mass flux caused by gas slippage, kg/s; $J_{k,om}$ is the mass flux due to Knudsen diffusion, kg/s; and $J_{sf,om}$ is the mass flux due to surface diffusion, kg/s. The expressions for the three terms of mass flux on the right hand side of Eq. (24) are given by (Zhang and Emami-Meybodi, 2021a).

The total mass flux of oil in organic pores ($J_{o,om}$) can be obtained by considering multiple oil storage and transport mechanisms, including the spatial variation of fluid characteristics in nanopores and the slippage effect (Zhang and Emami-Meybodi, 2021b):

where $R_{om}=R_{om,i}\exp[0.5(C_m-\gamma_m)(p_{mi}-p_m)]$ is the organic pore radius with the consideration of pressure-dependent porosity and permeability, m; $\rho_{o,m}$ and $\rho_{o,om}$ are the density of oil phase in bulk and near-wall region, kg/m^3; $\delta_{o,om}$ is the thickness of near-wall region, m; $\mu_{o,m}$ and $\mu_{o,om}$ are the viscosity of oil in bulk and near-wall region, respectively, cP; and $\lambda_{o,om}$ is the oil slip length in near-wall region of organic nanopores, m.

To incorporate the multiple fluid transport mechanisms into the

flow equation, we formulated the apparent permeability of organic matter based on the mass flux of oil or gas (hydrocarbon phase abbreviated with subscript h):

$$k_{\mathrm{h,om}} = 2.76 \times 10^{6} \frac{\phi_{\mathrm{om}}}{\tau_{\mathrm{om}}} \frac{J_{\mathrm{j,om}}}{\pi R_{\mathrm{om}}^{2}} \frac{\mu_{\mathrm{j,m}}}{\rho_{\mathrm{j,m}}} \frac{\partial y}{\partial p_{\mathrm{m}}}, \tag{26}$$

where ϕ_{om} is the porosity of organic matter; τ_{om} is the tortuosity; $k_{\mathrm{h,om}}$ is the apparent permeability of the organic matter, mD.

2.3.2. Inorganic pores

Due to the hydrophilicity of the inorganic matter, the inorganic pores contain both hydrocarbon and water, in which hydrocarbon occupies the bulk region, and the water phase adheres to the near-wall region (Shu et al., 2017). According to the Hagen-Poiseulle equation, the flow equations considering slippage effect are established for the hydrocarbon and water phase:

$$v_{\mathrm{bh}}(r) = 525517.24 \frac{\partial p_{\mathrm{m}}}{\partial y} \frac{R_{\mathrm{im}}^{2} - r^{2}}{\mu_{\mathrm{h,m}}} + c_{1}, \ 0 \le r \le R_{\mathrm{im}} - \delta_{\mathrm{w,im}}, \tag{27}$$

$$v_{\mathrm{nw}}(r) = 525517.24 \frac{\partial p_{\mathrm{m}}}{\partial y} \frac{R_{\mathrm{im}}^{2} - r^{2}}{\mu_{\mathrm{w,im}}} + c_{2}, \ R_{\mathrm{im}} - \delta_{\mathrm{w,im}} \le r \le R_{\mathrm{im}}, \tag{28}$$

where $R_{\mathrm{im}} = R_{\mathrm{im,i}} \exp[0.5(C_{\mathrm{m}} - \gamma_{\mathrm{m}})(p_{\mathrm{mi}} - p_{\mathrm{m}})]$ is the inorganic pore radius with the consideration of pressure-dependent porosity and permeability, m; v_{bh} and v_{nw} represent the velocity of hydrocarbon in the bulk region and water in near-wall region, respectively, m/s; $\mu_{\mathrm{h,m}}$ and $\mu_{\mathrm{w,im}}$ are the viscosity of hydrocarbon in bulk region and water in near-wall region, cP; $\delta_{\mathrm{w,im}}$ is the thickness of near-wall region, m; and c_1 and c_2 are constants to be calculated.

Considering the slippage effect on the interface of the bulk region and near-wall region, we developed the inner and outer boundary situations of the flow equation as follows:

$$\left. \frac{\partial v_{\mathrm{bh}}}{\partial r} \right|_{r=0} = 0, \tag{29}$$

$$v_{\mathrm{bh}}|_{r=R_{\mathrm{im}}-\delta_{\mathrm{w,im}}} = v_{\mathrm{nw}}|_{r=R_{\mathrm{im}}-\delta_{\mathrm{w,im}}} + v_{\mathrm{sh}}, \tag{30}$$

$$v_{\mathrm{nw}}|_{r=R_{\mathrm{im}}} = 0, \tag{31}$$

where v_{sh} is the slip velocity between water and hydrocarbon on the interface of bulk and near-wall region, which can be approximated by the slippage velocity on the solid interface (Shu et al., 2017):

$$v_{\mathrm{sg}} = -\frac{2 - \delta_{\mathrm{v}}}{\delta_{\mathrm{v}}} \lambda_{\mathrm{g}} \left(\frac{\partial v_{\mathrm{bg}}}{\partial r} \right) \Big|_{r=R_{\mathrm{im}}-\delta_{\mathrm{w,im}}}, \tag{32}$$

$$v_{\mathrm{so}} = -\lambda_{\mathrm{o}} \left(\frac{\partial v_{\mathrm{bo}}}{\partial r} \right) \Big|_{r=R_{\mathrm{im}}-\delta_{\mathrm{w,im}}}, \tag{33}$$

where δ_{v} is the regulation coefficient of tangential momentum, which is usually 1 for diffuse reflection; λ_{g} is the average free path of gas, m; and λ_{o} is the oil slip length at an interface between the bulk and near-wall region, m, and it can be approximated by $\lambda_{\mathrm{o}} = 10^{-9} \times [0.387\exp(-2 \times 10^{9} R_{\mathrm{im}}/32.47 + 0.74)]$.

By substituting Eqs. (27)–(28) into Eqs. (29)–(31), the velocity profiles of hydrocarbon and water in bulk and near-wall region of inorganic pores are given by:

$$v_{\mathrm{bh}}(r) = 2.26 \times 10^{7} \left[\frac{\partial p_{\mathrm{m}}}{\partial y} \frac{R_{\mathrm{im}}^{2} - r^{2}}{4\mu_{\mathrm{h,m}}} + \frac{\partial p_{\mathrm{m}}}{\partial y} \frac{R_{\mathrm{im}}^{2} - (R_{\mathrm{im}} - \delta_{\mathrm{w,im}})^{2}}{4} \frac{\mu_{\mathrm{h,m}} - \mu_{\mathrm{w,im}}}{\mu_{\mathrm{w,im}}\mu_{\mathrm{h,m}}} + \lambda_{\mathrm{h}} \frac{\partial p_{\mathrm{m}}}{\partial y} \frac{(R_{\mathrm{im}} - \delta_{\mathrm{w,im}})}{2\mu_{\mathrm{h,m}}} \right], \quad 0 \le r \le R_{\mathrm{im}} - \delta_{\mathrm{w,im}}, \tag{34}$$

$$v_{\mathrm{nw}}(r) = 2.26 \times 10^{7} \frac{\partial p_{\mathrm{m}}}{\partial y} \frac{R_{\mathrm{im}}^{2} - r^{2}}{4\mu_{\mathrm{w,im}}}, \ R_{\mathrm{im}} - \delta_{\mathrm{w,im}} \le r \le R_{\mathrm{im}}, \tag{35}$$

By integrating velocity profiles from 0 to $R_{\mathrm{im}} - \delta_{\mathrm{w,im}}$ for the bulk region, and the velocity profile from $R_{\mathrm{im}} - \delta_{\mathrm{w,im}}$ to R_{im} for the near-wall region, volume flux of hydrocarbon and water can be obtained, and the mass flux for the two regions can be written as:

$$\begin{aligned} J_{\mathrm{bh,im}} &= \rho_{\mathrm{h,m}} \int_{0}^{R_{\mathrm{im}}-\delta_{\mathrm{w,im}}} v_{\mathrm{bh}} \cdot 2\pi r \mathrm{d}r \\ &= 3.62 \times 10^{8} \rho_{\mathrm{h,m}} \pi \frac{\partial p_{\mathrm{m}}}{\partial y} (R_{\mathrm{im}} - \delta_{\mathrm{w,im}})^{2} \left[\frac{R_{\mathrm{im}}^{2} + 2R_{\mathrm{im}}\delta_{\mathrm{w,im}} - \delta_{\mathrm{w,im}}^{2}}{8\mu_{\mathrm{h,m}}} + \frac{2R_{\mathrm{im}}\delta_{\mathrm{w,im}} - \delta_{\mathrm{w,im}}^{2}}{4\mu_{\mathrm{h,m}}} \frac{\mu_{\mathrm{h,m}} - \mu_{\mathrm{w,im}}}{\mu_{\mathrm{w,im}}} + \lambda_{\mathrm{h}} \frac{(R_{\mathrm{im}} - \delta_{\mathrm{w,im}})}{2\mu_{\mathrm{h,m}}} \right], \end{aligned} \tag{36}$$

$$J_{\mathrm{nw,im}} = \rho_{\mathrm{w,im}} \int_{R_{\mathrm{im}}-\delta_{\mathrm{w,im}}}^{R_{\mathrm{im}}} v_{\mathrm{nw}} \cdot 2\pi r \mathrm{d}r = 3.62 \times 10^{8} \frac{\rho_{\mathrm{w,im}} \pi \left(2R_{\mathrm{im}}\delta_{\mathrm{w,im}} - \delta_{\mathrm{w,im}}^{2} \right)^{2}}{8\mu_{\mathrm{w,im}}} \frac{\partial p_{\mathrm{m}}}{\partial y}, \tag{37}$$

where $\rho_{h,m}$ and $\rho_{w,im}$ are the hydrocarbon density in the bulk region and water density in the near-wall region, kg/m^3; $J_{bh,im}$ is the hydrocarbon mass flux in inorganic nanopores, kg/s; and $J_{nw,im}$ is the water mass flux in inorganic pores, kg/s.

To incorporate the multiple fluid transport mechanisms into the flow equation, we obtained the apparent permeability of inorganic matter as a function of hydrocarbon mass flux:

$$k_{h,im} = 2.76 \times 10^6 \frac{\phi_{im}}{\tau_{im}} \frac{J_{bh,im}}{\pi R_{im}^2} \frac{\mu_{h,m}}{\rho_{h,m}} \frac{\partial y}{\partial p_m}, \tag{38}$$

where ϕ_{im} is the inorganic porosity; τ_{im} is the tortuosity of nanopores in inorganic materials; and $k_{h,im}$ is the inorganic apparent relative permeability.

Based on the assumption that organic and inorganic nanopores were arranged in parallel with no mass exchange between them, the total apparent permeability of hydrocarbon in the matrix can be expressed as:

$$k_{h,m} = \psi k_{h,om} + (1-\psi) k_{h,im}, \tag{39}$$

where ψ is the volume fraction of organic matter in the matrix.

Since water in the matrix only exists in inorganic pores, the total apparent permeability of water is as follows:

$$k_{w,m} = k_{w,im} = 2.76 \times 10^6 \frac{\phi_{im}}{\tau_{im}} \frac{J_{nw,im}}{\pi R_{im}^2} \frac{\mu_{w,im}}{\rho_{w,im}} \frac{\partial y}{\partial p_m} = 10^{15} \frac{\left(2R_{im}\delta_{w,im} - \delta_{w,im}^2\right)^2}{8R_{im}^2} \frac{\phi_{im}}{\tau_{im}}. \tag{40}$$

The water layer thickness $\delta_{w,im}$ in Eq. (40) is related to the matrix water saturation, which is calculated using the material balance equations. The two-phase storage and transport mechanisms affect the calculation of dimensionless time and pseudotime, which further affect the behavior of type curve and data plot.

2.4. Type-curve workflow

The proposed type-curve method is based on the pseudopressure and pseudotime variables (Table 1). To calculate pseudopressure and pseudotime, the relationship between average pressure and water saturation should be first obtained using material balance equations in the fracture and the distance of investigation (DOI) in the matrix (Zhang and Emami-Meybodi, 2022):

$$Q_w = V_{fi}\left(\frac{S_{w,fi}}{B_{w,fi}} - \frac{\overline{S}_{w,f}}{\overline{B}_{w,f}}\left[1 - C_f\left(p_{fi} - \overline{p}_f\right)\right]\right) + Q_{sw}, \tag{41}$$

$$Q_h = V_{fi}\left(\frac{S_{h,fi}}{B_{h,fi}} - \frac{\overline{S}_{h,f}}{\overline{B}_{h,f}}\left[1 - C_f\left(p_{fi} - \overline{p}_f\right)\right]\right) + Q_{sh}, \tag{42}$$

$$Q_{sw} = V_{w,mi}\left(\frac{S_{w,mi}}{B_{w,mi}} - \frac{\overline{S}_{w,m}}{\overline{B}_{w,m}}\left[1 - C_m(p_{mi} - \overline{p}_m)\right]\right), \tag{43}$$

$$Q_{sh} = V_{h,mi}\left(\frac{S_{h,mi}}{B_{h,mi}} - \frac{\overline{S}_{hc,m}}{\overline{B}_{hc,m}}\left[1 - C_m(p_{mi} - \overline{p}_m)\right]\right), \tag{44}$$

$$\overline{S}_{w,f} + \overline{S}_{h,f} = 1, \tag{45}$$

$$\overline{S}_{w,m} + \overline{S}_{h,m} = 1, \tag{46}$$

where subscript h represents hydrocarbon (h can be o = oil or g = gas); Q_h and Q_w are the cumulative hydrocarbon and water production at the surface condition, STB; Q_{sh} and Q_{sw} are the cumulative hydrocarbon and water influx from the matrix, STB; $\overline{p}_m$ is the average pressure of matrix DOI, psi; and $\overline{S}_{j,f}$ and $\overline{S}_{j,m}$ are the average saturation in fracture and the matrix DOI, respectively.

V_{fi} and $V_{j,mi}$ are the initial pore-volume of fracture and quarter element in the matrix DOI, respectively:

$$V_{fi} = 2x_f w_f h \phi_{fi}, \tag{47}$$

$$V_{j,mi} = y_j x_f h \phi_{mi}, \tag{48}$$

$$y_j = 0.194 \sqrt{\frac{k_{mi} t_{pj,m}}{\left(\phi_m \mu_{j,m} C_{ej,m}\right)_i}}, \tag{49}$$

where y_j is the matrix DOI, ft.

The formation volume factors can be obtained using:

$$\overline{B}_w = B_{wi}[1 + C_w(p_i - \overline{p})], \quad \overline{B}_o = B_{oi}[1 + C_o(p_i - \overline{p})], \tag{50}$$

$$\overline{B}_g = \frac{p_{sc} T}{T_{sc}} \frac{\overline{Z}}{\overline{p}}. \tag{51}$$

We can establish the six material balance equations for either shale oil or gas. For each time step, we used the fixed-point iteration arithmetic to simultaneously solve the six unknowns (i.e., $\overline{p}_f$, $\overline{p}_m$, $\overline{S}_{w,f}$, $\overline{S}_{hc,f}$, $\overline{S}_{w,m}$, and $\overline{S}_{hc,m}$), then calculate the pseudopressure and pseudotime.

V_{fi} is an input parameter for solving the material balance eqautions, which is an unknown that needs to be determined in the type-curve analysis. Therefore, we used an iterative workflow to estimate HF properties. For simplicity, we defined the four parameters *RNP*, *PNR*, *DRNP*, and d*RNP* in Eqs. (52)–(54).

$$RNP = \frac{m_f(p_{fi}) - m_f(p_{wf})}{q}, \quad PNR = \frac{q}{m_f(p_{fi}) - m_f(p_{wf})}, \tag{52}$$

$$DRNP = \frac{dRNP}{d\ln t_{sp}}, \tag{53}$$

$$dRNP = \frac{dRNP}{dt_{sp}}. \tag{54}$$

where *RNP* is the rate normalized pseudopressure, (psi day)/STB; *PNR* is the pseudopressure normalized rate, STB/day/psi; *DRNP* is

Table 2
The V_{fi} and k_{fi} formulas based on the type curve are summarized.

Type curves	$\left(\frac{2x_f}{w_f}\right)\frac{1}{p_{wD}}$ vs. t_D	$\left(\frac{2x_f}{w_f}\right)\frac{1}{d\ln p_{wD}}$ vs. t_D	$\left(\frac{w_f}{2x_f}\right)p_{wD}'$ vs. t_D
Data plot	PNR vs. t_{sp}	$1/DRNP$ vs. t_{sp}	$dRNP$ vs. t_{sp}
V_{fi}	$V_{fi} = \frac{4\beta\alpha_j B_{fi} X_{MP} Y_{MP}}{(C_{e,f})_i}$		$V_{fi} = \frac{4\beta\alpha_j B_{fi}}{(C_{e,f})_i Y_{MP}}$
k_{fi}	$k_{fi} = \frac{4\beta\alpha_j^2 B_{fi}^2 \mu_{fi} X_{MP} Y_{MP}^2}{(w_f h)^2 (\phi_f C_{e,f})_i}$		$k_{fi} = \frac{4\beta\alpha_j^2 B_{fi}^2 (\mu_f)_i}{(w_f h)^2 (\phi_f C_{e,f})_i Y_{MP}^2 X_{MP}}$

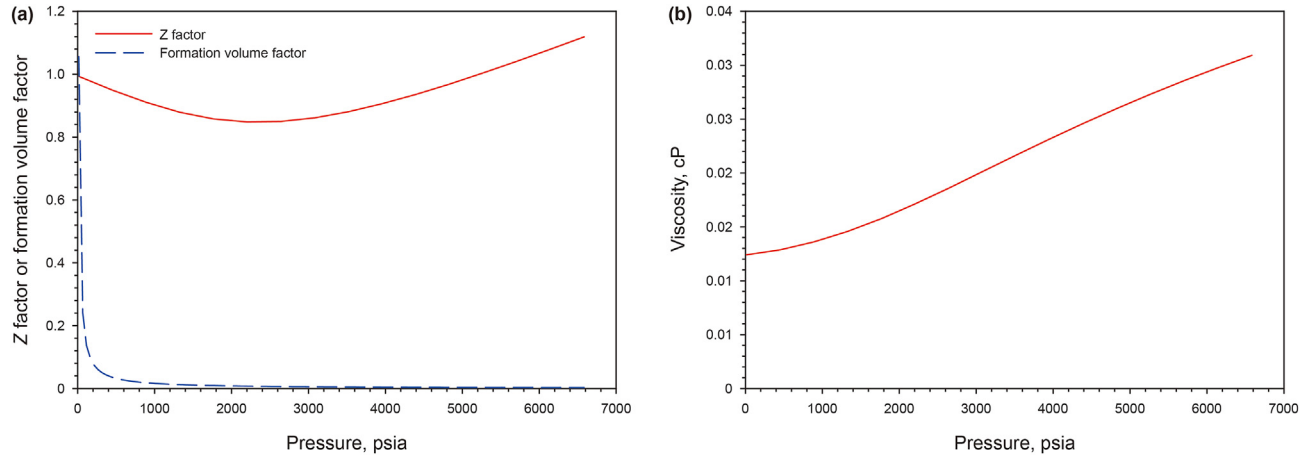

Fig. 3. Gas properties plot: (**a**) *Z* factor and formation volume factor versus pressure; (**b**) Gas viscosity versus pressure.

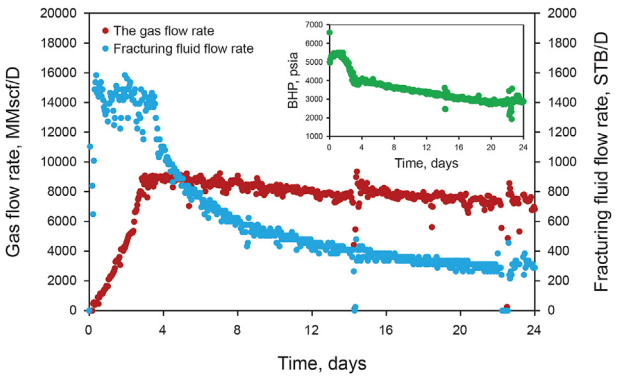

Fig. 4. Gas flowrate, water flowrate, and BHP history plot.

the derivative of *RNP* with respect to $\ln t_{sp}$; and *dRNP* is the derivative of *RNP* with respect to t_{sp}.

The iterative workflow was established in seven steps as follows:

(1) Collect the fluid properties (μ, C, B, etc.), production data (q, p_{wf}, t), and reservoir properties (p_i, ϕ_{mi}, k_{mi}, C_m, etc.). Field production data are screened on Cartesian plots, semi-logarithmic plots, and log-log plots to reduce matching errors.
(2) Assume an initial guess of V_{fi} and γ_f.
(3) Generate type-curves of $(2x_f/w_f)/p_{wD}$, $(w_f/2x_f)p_{wD}'$, and $(2x_f/w_f)/d\ln p_{wD}'$ for water and hydrocarbon using Eq. (15), where x_f is calculated based on V_{fi} in Eq. (47).
(4) Generate "data plots" for water and hydrocarbon:
   a. Estimate $\bar{p}_f$, $\bar{p}_m$, $\bar{S}_f$, and $\bar{S}_m$ by solving material balance equation from Eqs. (41)–(46).
   b. Evalulate *PNR* and t_{sp} with the pressure-saturation relationship obtained from the material balance equations.
   c. Plot $1/DRNP$, *PNR*, and *dRNP* with t_{sp} in log-log scale as "data plots".
(5) Force match type curve with data plot and estimate fracture parameters:
   a. "Force" match type curve with data plot. Choose any match point on the overlapping portion of the curve (usually choose the point on the portion of fracture BDF because of its unique behavior).
   b. Record the values of y-axis pairs $\left[\left(\frac{2x_f}{w_f}\right)\frac{1}{d\ln p_{wD}}\right]_{MP} - \left[\frac{1}{DRNP}\right]_{MP}$, $\left[\left(\frac{2x_f}{w_f}\right)\frac{1}{p_{wD}}\right]_{MP} - [PNR]_{MP}$, and $\left[\left(\frac{w_f}{2x_f}\right)p_{wD}'\right]_{MP} - [dRNP]_{MP}$ and x-axis pair $[t_D]_{MP} - [t_{sp}]_{MP}$ from both data plot and type curve.
   c. According to Eqs. (55)–(58), define X_{MP} as the ratio of $[t_{sp}]_{MP}$ to $[t_D]_{MP}$ and define Y_{MP} as the ratio of the y axis pairs of data plot to type curve.
   d. Determine $V_{fi,w}$ and $k_{fi,w}$ from water phase plots and $V_{fi,h}$ and $k_{fi,h}$ from hydrocarbon phase plots using the equations listed in Table 2.
(6) Compare the interpreted V_{fi} with the initial iteration value. If the relative error is greater than the set tolerance, the newly calculated V_{fi} is substituted back to Step 2 as the initial value of iteration. If the relative error is less than the specified tolerance, the iteration of V_{fi} converges.
(7) Check the convergence of k_f by comparing the calculated $k_{fi,w}$ and $k_{fi,h}$. If the relative error between $k_{fi,w}$ and $k_{fi,h}$ is larger than the set tolerance, update γ_f with another value from

Table 3
Input data for Marcellus shale Wells (Zhang and Emami-Meybodi, 2021a).

Parameters	Values
Initial pressure of the fracture and matrix for flowback p_{fi} and p_{mi}, psi	6,580
Initial pressure of the fracture and matrix for long time production p_{ri}, psi	4,480
Temperature T, °F	140
Specific gravity	0.6
Water compressibility C_w, psi^{-1}	2.4×10^{-6}
Initial fracture porosity ϕ_{fi}, %	60
Initial matrix porosity ϕ_{mi}, %	7.75
Matrix compressibility C_m, psi^{-1}	1×10^{-6}
Matrix permeability modulus γ_m, psi^{-1}	0
Water formation-volume-factor at initial pressure B_{wi}, ft^3/STB	5.78
Initial fracture water saturation $S_{w,fi}$, %	98
Initial matrix water saturation $S_{w,mi}$, %	28
Water viscosity μ_w, cP	0.54
Water density ρ_w, lb/ft^3	62
Reservoir thickness h, ft	80
Number of active fractures	66
Fracture half spacing y_m, ft	40
Fracture width w_f, ft	0.04

10^{-4} to 10^{-3} psi^{-1} (Ozkan et al., 2010). When k_f converges, output the calculated V_{fi}, k_{fi}, and γ_f as interpretation results.

$$(t_D)_{MP} = \frac{\beta\eta_{j,f}}{x_f^2}(t_{sp})_{MP}, \tag{55}$$

$$\left[\left(\frac{2x_f}{w_f}\right)\frac{1}{p_{wD}}\right]_{MP} = \frac{2x_f\alpha_j\mu_{fi}B_{fi}}{w_f k_{fi} h}[PNR]_{MP}, \tag{56}$$

$$\left[\left(\frac{2x_f}{w_f}\right)\frac{1}{\mathrm{dln}p_{wD}}\right]_{MP} = \frac{2x_f\alpha_j\mu_{fi}B_{fi}}{w_f k_{fi} h}\left[\frac{1}{DRNP}\right]_{MP}, \tag{57}$$

$$\left[\left(\frac{w_f}{2x_f}\right)p'_{wD}\right]_{MP} = \frac{w_f k_{fi} h}{2x_f\alpha_j\mu_{fi}B_{fi}}\frac{x_f^2}{\beta\eta_f}[dRNP]_{MP}. \tag{58}$$

3. Results

We applied the proposed type-curve method to an MFHW in the Marcellus shale gas reservoir. The semianalytical model and workflow proposed in this study are used to analyze the flowback data of this well, characterize the HF properties, as well as provide technical guidance and adjustment for production & operations. The well was fractured in 22 stages. Each stage contains five clusters. This was followed by 24 days of flowback and eight months of continuous production. The BHP, production history, and the input parameters required for HF characterization were provided by Zhang and Emami-Meybodi (2021a). After four days of flowback, the gas flow rate stabilized at around 8,000 STB/day, while the fracturing fluid flow rate continued to decrease. During the period from the beginning of flowback to 24 days of flowback, the fracturing fluid flow rate decreased from 2,660 to 200 STB/day.

Initially, this field example was analyzed using the two-phase straight-line analysis method (Zhang and Emami-Meybodi, 2021a) and the type-curve method (Zhang and Emami-Meybodi, 2022). However, both of these works ignored the multiple fluid storage and transport mechanisms. While the former study considers the transport mechanism into the straight-line analysis (Zhang and Emami-Meybodi, 2021a), the assumption of single-phase gas flow in the matrix still limits the accuracy of the interpretation results. Furthermore, the latter study didn't consider transport mechanisms in the type-curve analysis. Therefore, we revisited this field example to exhibit the applicability of the proposed method.

We followed the iterative workflow proposed in the previous section and exhibit the analysis process step by step as follows:

(1) Collect the fluid properties (μ, Z, B) in Fig. 3, production data (q, p_{wf}, t) in Fig. 4, and reservoir properties (p_i, ϕ_{mi}, k_{mi}, C_m, etc.) in Table 3.
(2) An initial guess of $V_{fi} = 200$ Mcf and $\gamma_f = 1 \times 10^{-4}$ psi^{-1} are given to start the iteration.
(3)–(4) With the initial guess of V_{fi} and γ_f, the type curves and data plots are generated for water and gas phase, respectively. The type curves of $(2x_f/w_f)/p_{wD}$ and $(2x_f/w_f)/\mathrm{dln}p_{wD}'$ and the data plots of *PNR* and 1/*DRNP* for gas phase are shown in Fig. 5a. Fig. 5b shows the type curve of $(2x_f/w_f)/p_{wD}$ and $(2x_f/w_f)/\mathrm{dln}p_{wD}'$ and the data plots of *PNR* and 1/*DRNP* for the water phase.
(5) Due to the significant fluctuation of the derivative plot 1/*DRNP*, the *PNR* plot is used to match with the type curve of $(2x_f/w_f)/p_{wD}$ by moving the plot manually. We selected a match point at $t_D = 0.3$ for gas phase and $t_D = 1$ for water phase, and calculated the x-axis ratio X_{MP} and y-axis ratio Y_{MP}. According to Table 2 and the calculated X_{MP} and Y_{MP},

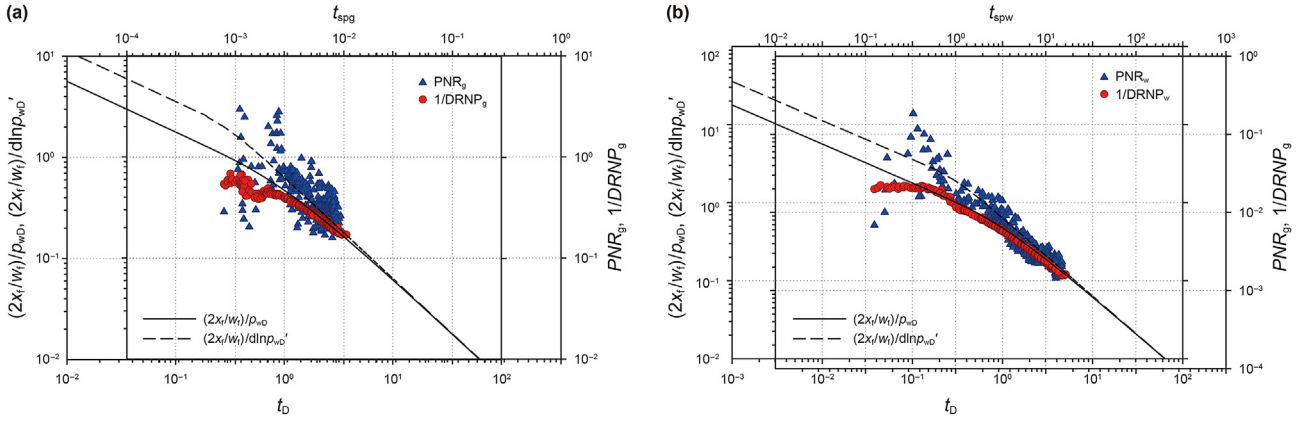

Fig. 5. Flowback analysis plots: (**a**) The type curves of $(2x_f/w_f)/p_{wD}$ and $(2x_f/w_f)/\mathrm{dln}p_{wD}'$ and data plots for gas phase; (**b**) The type curves of $(2x_f/w_f)/p_{wD}$ and $(2x_f/w_f)/\mathrm{dln}p_{wD}'$ and data plots for water phase.

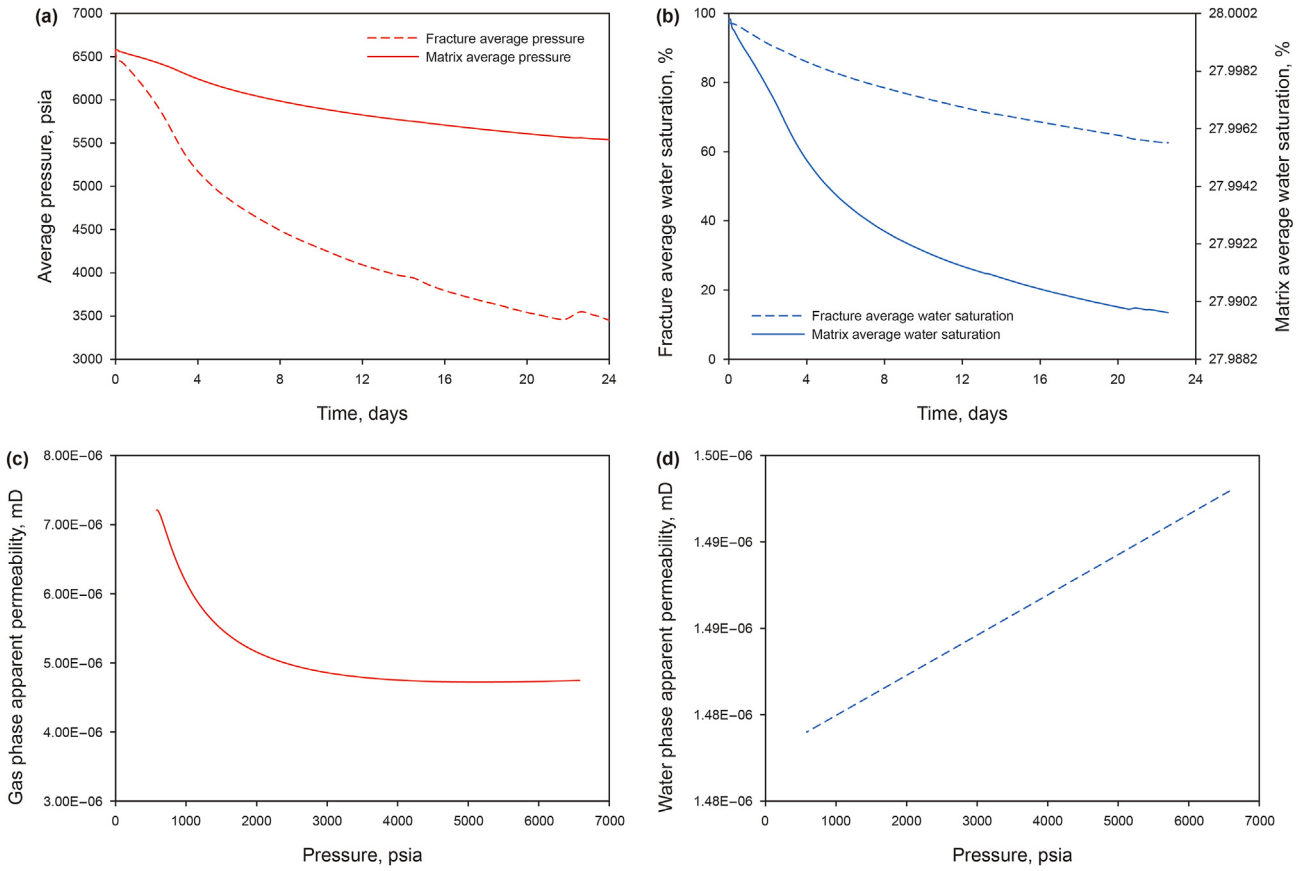

Fig. 6. Flowback analysis plots: (**a**) Average pressure in the fracture and average pressure in the DOI of matrix; (**b**) Average saturation of water in fracture and DOI of matrix; (**c**) Apparent permeability for gas phase; (**d**) Apparent permeability for water phase.

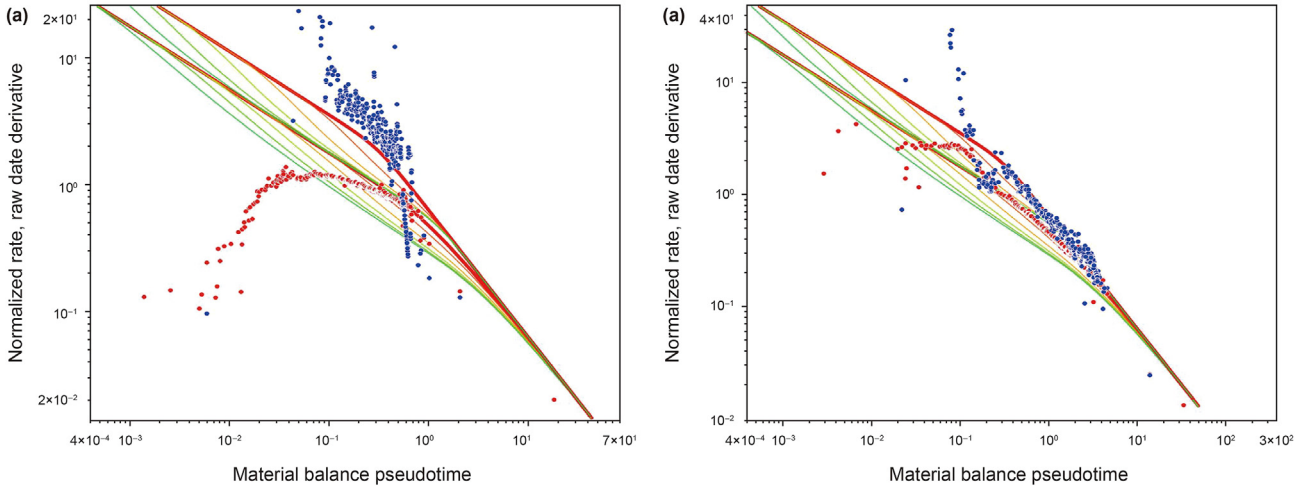

Fig. 7. Flowback analysis using Wattenbarger type curve developed for single phase: (**a**) Type curve and data plot for gas phase; (**b**) Type curve and data plot for water phase.

$V_{fi,w}$ = 176.65 Mcf and $k_{fi,w}$ = 341 mD are calculated for water phase and $V_{fi,g}$ = 121.40 Mcf and $k_{fi,g}$ = 352 mD for gas phase. The two-phase storage and transport mechanisms are considered in the calculation of matrix influx to the fracture.

(6) By comparing the interpreted V_{fi} in Step (5) with the initial guess in Step (2), the relative error is larger than the set tolerance of 10%. Therefore, the newly calculated V_{fi} is substituted back to Step (2) to continue the iteration.

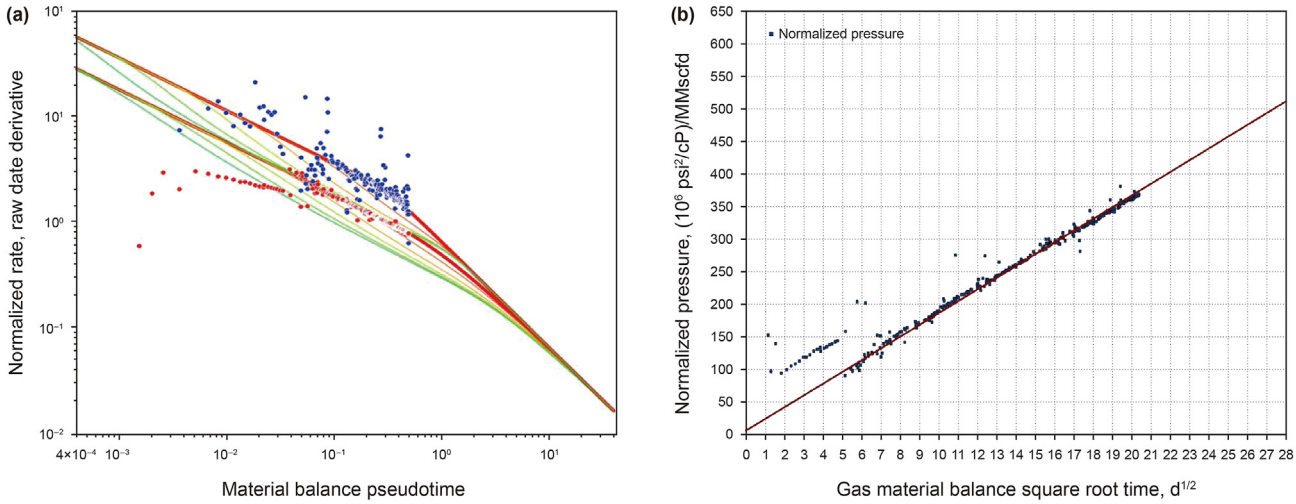

Fig. 8. Long-term production data analysis plots: (**a**) Wattenbarger type curve analysis; (**b**) Straight line analysis.

Table 4
Fracturing fluid flowback data interpretation results.

Fracture parameters	Flowback interpretation results		Long time production data analysis for single phase gas		
	Water phase	Gas phase	History match (Zhang and Emami-Meybodi, 2021a)	Straight line analysis	Type curve analysis
k_{fi}, mD	389	372	–	–	–
V_{fi}, Mcf	159.44	164.85	–	–	–
γ_f, psi^{-1}	1×10^{-4}	–	–	–	–
C_f, psi^{-1}	6×10^{-5}	–	–	–	–
Final k_f, mD	16.6	–	46.4	–	–
Final V_f, Mcf	125.1	–	123.9	109.7	119.0

(7) After convergence, we obtained the final interpretation results of fracture pore volume and permeability: $V_{fi,g}$ and $k_{fi,g}$ were 164.85 Mcf and 372 mD for gas phase and $V_{fi,w}$ and $k_{fi,w}$ were 159.44 Mcf and 389.0 mD for water phase. The relative errors for V_{fi} and k_{fi} were 0.2% and 1.7% between gas and water phases data.

After V_{fi} converges, the average fracture pressure and average water saturation curve are obtained in Fig. 6a and b, which reveal that the initial production was dominated by fracture flow and the long-term production was dominated by matrix flow. Fig. 6c and d show the variation of apparent permeability for gas and water caused by the two-phase storage and transport mechanisms. It is observed that the apparent permeability for gas phase increases as pressure decreases, which agrees with the observation obtained from Zhang and Emami-Meybodi (2021a). The apparent permeability for the water phase decreases as pressure decreases, which is consistent with the understanding from field examples that the fracturing fluid invaded into the formation during the late flowback period.

To illustrate the superiority of the proposed type curve in two-phase flowback analysis, we used Wattenbarger type curve, which is developed for single-phase flow, to attempt the two-phase flowback analysis. The gas flowrate, water flowrate and BHP history in Fig. 4 are respectively used to generate the water-phase and gas-phase data plot. As shown in Fig. 7, the water-phase data plot shows a good match with type curve with the calculated $V_{fi} = 96.5$ Mcf. This is because during flowback period water dominates the production. But the interpreted V_{fi} contains large error due to the single-phase assumption. Whereas, the gas-phase data plot cannot be matched with type curve not matter how we move with each other. Because the behavior of two phase during flowback lead to significant nonlinearity in gas-phase pseudotime and RNP. The earlier the flowback data are, the more nonlinear the data plot is and the more deviation from the straight line there is. The comparison between Figs. 5 and 7 illustrates the superiority and robustness of the proposed type curve in two-phase flowback analysis.

Zhang and Emami-Meybodi (2021a) used the history matching process to obtain the fracture pore-volume $V_f = 123.9$ Mcf and fracture permeability $k_f = 46.4$ mD based on long-term production data. This study also uses straight-line analysis and Wattenbarger type curve that are both developed for single phase to estimate fracture pore-volume during production (see Fig. 8). The calculated $V_f = 109.7$ Mcf for straight-line analysis and $V_f = 119.0$ Mcf for type-curve analysis show good consistence with history matching results. Although the estimated V_f using single-phase type curve exhibits significant difference with the estimated V_{fi} using the proposed two-phase type curve, the interpretation results of production data provided a significant constraint of HF dynamics due to fracture closure, which was characterized by C_f and γ_f. By reconciling the flowback and production data, the C_f and γ_f were obtained to be 6×10^{-5} psi^{-1} and 1×10^{-4} psi^{-1}, respectively. The V_f and k_f under the final condition were 125.1 Mcf and 16.6 mD

using the exponential relationship based on the flowback data. The predicted HF properties using flowback data are in good agreement with the HF properties obtained from the history matching of long-term production data. The interpretation results for this field example are shown in Table 4.

4. Conclusions

We proposed a two-phase flowback type-curve method for multiscale fluid transport in shale reservoirs to evaluate HF performance and estimate HF properties. The main conclusions are as follows:

(1) The type-curve method can be used to analyze flowback data from MFHWs in shale reservoirs. The type-curve method considers two-phase hydrocarbon-water storage and transport mechanisms, including diffusion, slippage, and adsorption.
(2) The multiscale fluid transport mechanisms are incorporated into the dimensionless groups by defining a new group of dimensionless parameters. The chosen parameters provide a single line type curve for extracting HF properties. The early time negative half-slope straight line of the type curve represents the HF IALF regime, and the negative unit-slope straight line denotes the BDF regime of fracture.
(3) The analysis of the field example shows that due to the two-phase storage and transport mechanism, the apparent permeabilities of gas and water phases show different variation trends with the decrease of pressure. Such an observation is consistent with the field observation, implying that it is challenging to produce the injected fracturing fluid from the formation.

Declaration of competing interest

The authors declare that they have no known competing financial interests or personal relationships that could have appeared to influence the work reported in this paper.

Acknowledgments

This research is supported by National Natural Science Foundation of China (No. 52204057), and the Science Foundation of China University of Petroleum, Beijing (No. 2462021BJRC003 and 2462021YJRC012).

References

Abbasi, M.A., Dehghanpour, H., Hawkes, R.V., 2012. Flowback analysis for fracture characterization. In: SPE Canadian Unconventional Resources Conference. https://doi.org/10.2118/162661-MS.
Agarwal, R.G., Gardner, D.C., Kleinsteiber, S.W., Fussell, D.D., 1999. Analyzing well production data using combined-type-curve and decline-curve analysis concepts. SPE Reservoir Eval. Eng. 2 (5), 478–486. https://doi.org/10.2118/57916-PA.
Barzin, Y., Mattar, L., 2017. Limitations of current type curves in characterizing SRV; and development of EFR type curves. In: SPE Unconventional Resources Conference. https://doi.org/10.2118/185038-MS.
Beskok, A., Karniadakis, G.E., Trimmer, W., 1996. Rarefaction and compressibility effects in gas microflows. J. Fluids Eng. Trans. ASME. 118 (5), 448–456. https://doi.org/10.1115/1.2817779.
Bourdet, D., Ayoub, J.A., Pirard, Y.M., 1989. Use of pressure derivative in well test interpretation. SPE Form. Eval. 4 (2), 293–302. https://doi.org/10.2118/12777-PA.
Cao, L., Sun, J., Liu, J., Liu, J., 2022a. Experiment and application of wax deposition in dabei deep condensate gas wells with high pressure. Energies 15, 6200. https://doi.org/10.3390/en15176200.
Cao, L., Sun, J., Zhang, B., Lu, N., Xu, Y., 2022b. Sensitivity analysis of the temperature profile changing law in the production string of a high-pressure high-temperature gas well considering the coupling relation among the gas flow friction, gas properties, temperature, and pressure. Front. Physiol. 10, 1112. https://doi.org/10.3389/fphy.2022.1050229.
Carter, R.D., 1985. Type curves for finite radial and linear gas-flow systems: constant-terminal-pressure case. SPE J. 25 (5), 719–728. https://doi.org/10.2118/12917-PA.
Clarkson, C.R., 2013. Production data analysis of unconventional gas wells: review of theory and best practices. Int. J. Coal Geol. 109–110 (1), 101–146. https://doi.org/10.1016/j.coal.2013.01.002.
Cui, J.F., 2019. Oil transport in shale nanopores and micro-fractures: modeling and analysis. J. Petrol. Sci. Eng. 178, 640–648. https://doi.org/10.1016/j.petrol.2019.03.088.
Cui, J., Sang, Q., Li, Y., Yin, C., Li, Y., Dong, M.J., 2017. Liquid permeability of organic nanopores in shale: calculation and analysis. Fuel 202 (15), 426–434. https://doi.org/10.1016/j.fuel.2017.04.057.
Fan, D., Ettehadtavakkol, A., Wang, W.D., 2020. Apparent liquid permeability in mixed-wet shale permeable media. Transport Porous Media 134 (3), 651–677. https://doi.org/10.1007/s11242-020-01462-5.
Fetkovich, M.J., 1980. Decline curve analysis using type curves. J. Petrol. Technol. 32 (6), 1065–1077. https://doi.org/10.2118/4629-PA.
Gao, J., Yu, Q.C., Lu, X., 2017. Apparent permeability and gas flow behavior in carboniferous shale from the Qaidam Basin, China: an experimental study. Transport Porous Media 116 (2), 585–611. https://doi.org/10.1007/s11242-016-0791-y.
Guo, T., Tang, S., Liu, S., Liu, X., Rui, 2021. Physical simulation of hydraulic fracturing of large-sized tight sandstone outcrops. SPE J. 26 (1), 372–393. https://doi.org/10.2118/204210-PA.
Guo, W., Hu, Z., Zuo, L., Gao, S., Yu, R., Zeng, B., 2015. Experimental study on desorption, diffusion and seepage coupling in shale matrix. Chinese J. Mechanics 47 (6), 916–922. https://doi.org/10.6052/0459-1879-15-068 (in Chinese).
Javadpour, F., 2009. Nanopores and apparent permeability of gas flow in mudrocks (shales and siltstone). J. Can. Pet. Technol. 48 (8), 16–21. https://doi.org/10.2118/09-08-16-DA.
Javadpour, F., Moghanloo, R.G., Davudov, D., 2013. Contribution of methane molecular diffusion in kerogen to gas-in-place and production. In: SPE Western Regional and AAPG Pacific Section Meeting 2013 Joint Technical Conference. https://doi.org/10.2118/165376-MS.
Javadpour, F., Mcclure, M., Naraghi, M.E., 2015. Slip-corrected liquid permeability and its effect on hydraulic fracturing and fluid loss in shale. Fuel 160 (15), 549–559. https://doi.org/10.1016/j.fuel.2015.08.017.
Klinkenberg, L.J., 1941. The permeability of porous media to liquids and gases. Drilling and Production Practice 2, 200–213. https://doi.org/10.5510/OGP20120200114.
Li, J., Li, X., Wu, K., Wang, X., Shi, J., Yang, L., Zhang, H., Sun, Z., Wang, R., Feng, D., 2016. Water sorption and distribution characteristics in clay and shale: effect of surface force. Energy Fuel. 30 (11), 8863–8874. https://doi.org/10.1021/acs.energyfuels.6b00927.
Li, Y., Kalantari-Dahaghi, A., Zolfaghari, A., Dong, P., Negahban, S., Zhou, D., 2020. A new model for the transport of gaseous hydrocarbon in shale nanopores coupling real gas effect, adsorption, and multiphase pore fluid occupancies. Int. J. Heat Mass Tran. 148, 119026. https://doi.org/10.1016/j.ijheatmasstransfer.2019.119026.
Lu, T., Li, Z., Lai, F., Meng, Y., Ma, W., Sun, Y., Wei, M., 2019. Blasingame decline analysis for variable rate/variable pressure drop: a multiple fractured horizontal well case in shale gas reservoirs. J. Petrol. Sci. Eng. 178, 193–204. https://doi.org/10.1016/j.petrol.2019.03.036.
Mehrotra, A.K., Svrcek, W.Y., 1982. Correlations for properties of bitumen saturated with CO_2 , CH_4 and N_2, and experiments with combustion gas mixtures. J. Can. Pet. Technol. 21 (6), 82. https://doi.org/10.2118/82-06-05, 06-05.
Mi, L., Jiang, H., Li, J., 2014a. The impact of diffusion type on multiscale discrete fracture model numerical simulation for shale gas. J. Nat. Gas Sci. Eng. 20, 74–81. https://doi.org/10.1016/j.jngse.2014.06.013.
Mi, L., Jiang, H., Li, J., Li, T., 2014b. Mechanism of the gas diffusion in shale reservoirs. Petroleum Geology and Development in Daqing 33 (1), 154–159 (in Chinese). https://10.3969/J.ISSN.1000-3754.2014.01.030.
Miller, F.G., 1962. Theory of unsteady-state influx of water in linear reservoirs. J. Inst. Petrol. 48 (467), 365–379.
Mohaghegh, S., Ertekin, T., 1991. A type-curve solution for coal seam degasification wells producing under two-phase flow conditions. In: SPE Annual Technical Conference and Exhibition. https://doi.org/10.2118/22673-MS.
Nobakht, M., Clarkson, C.R., Kaviani, D., 2013. New type curves for analyzing horizontal well with multiple fractures in shale gas reservoirs. J. Nat. Gas Sci. Eng. 10, 99–112. https://doi.org/10.1016/j.jngse.2012.09.002.
Orozco, D., Aguilera, R., 2015. A material balance equation for stress-sensitive shale gas reservoirs considering the contribution of free, adsorbed and dissolved gas. In: SPE/CSUR Unconventional Resources Conference. https://doi.org/10.2118/175964-MS.
Özısık, M.N., Ã–zisik, M.N., 1993. Heat Conduction. John Wiley & Sons.
Ozkan, E., Raghavan, R.S., Apaydin, O.G., 2010. Modeling of fluid transfer from shale matrix to fracture network. In: SPE Annual Technical Conference and Exhibition. https://doi.org/10.2118/134830-MS.
Palacio, J., Blasingame, T., 1993. Decline curve analysis using type curves: analysis of gas well production data. In: SPE Joint Rocky Mountain Rogional and Low Pereability Rosorvoirs Symposium. https://doi.org/10.2118/25909.
Shen, W., Li, X., Cihan, A., Lu, X., Liu, X., 2019. Experimental and numerical

simulation of water adsorption and diffusion in shale gas reservoir rocks. Adv. Gco-Energy Res. 3 (2), 165–174. https://doi.org/10.26804/ager.2019.02.06.
Sheng, M., Li, G., Huang, Z., 2014. Transient flow model of shale gas considering surface diffusion. Acta Petrol 35 (2), 347–352. https://doi.org/10.7623/syxb201402016 (in Chinese).
Shu, J.J., Ji, B., Chan, W.K., 2017. Fluid velocity slip and temperature jump at a solid surface. Appl. Mech. Rev. 69 (2), 020801. https://doi.org/10.1115/1.4036191.
Suhrer, M., Toelke, J., Diaz, E., Grader, A., Cespedes, S., 2013. Computed two-phase relative permeability using digital rock physics in a shale formation. In: SPE/AAPG/SEG Unconventional Resources Technology Conference. https://doi.org/10.1190/urtec2013-092.
Sun, J., Gamboa, E.S., Schechter, D., Rui, Z., 2016. An integrated workflow for characterization and simulation of complex fracture networks utilizing microseismic and horizontal core data. Crit. Care Med. 34, 1347–1360. https://doi.org/10.1016/j.jngse.2016.08.024.
Sun, Z., Li, X., Shi, J., Zhang, T., Sun, F., 2017. Apparent permeability model for real gas transport through shale gas reservoirs considering water distribution characteristic. Int. J. Heat Mass Tran. 115, 1008–1019. https://doi.org/10.1016/j.ijheatmasstransfer.2017.07.123.
Swami, V., Settari, A., 2012. A pore scale gas flow model for shale gas reservoir. In: SPE Americas Unconventional Resources Conference. https://doi.org/10.2118/155756-MS.
Swami, V., Settari, A., Javadpour, F., 2013. A numerical model for multi-mechanism flow in shale gas reservoirs with application to laboratory scale testing. In: EAGE Annual Conference & Exhibition Incorporating SPE Europec. https://doi.org/10.2118/164840-MS.
Tang, G.H., Tao, W.Q., He, Y.L., 2005. Gas slippage effect on microscale porous flow using the lattice Boltzmann method. Phys. Rev. E - Stat. Nonlinear Soft Matter Phys. 72 (5), 6301. https://doi.org/10.1103/PhysRevE.72.056301.
Tao, Z., Li, X., Jing, L., Dong, F., Song, H., 2018. A fractal model for gas–water relative permeability in inorganic shale with nanoscale pores. Transport Porous Media 122 (2), 305–331. https://doi.org/10.1007/s11242-018-1006-5.
Thararoop, P., Karpyn, Z.T., Ertekin, T., 2015. A production type-curve solution for coalbed methane reservoirs. J. Unconv. 9, 136–152. https://doi.org/10.1016/j.juogr.2014.12.001.
Wang, H., Marongiu-Porcu, M., 2015. Impact of shale gas apparent permeability on production: combined effects of non-Darcy flow/gas slippage, desorption, and geomechanics. SPE Reservoir Eval. Eng. 18 (4), 495–507. https://doi.org/10.2118/173196-PA.
Wang, H., Su, Y., Zhao, Z., Wang, W., Sheng, G., Zhan, S., 2019. Apparent permeability model for shale oil transport through elliptic nanopores considering wall-oil interaction. J. Petrol. Sci. Eng. 176, 1041–1052. https://doi.org/10.1016/j.petrol.2019.02.027.
Wang, J., Luo, H., Liu, H., Cao, F., Li, Z., Sepehrnoori, K., 2016. An integrative model to simulate gas transport and production coupled with gas adsorption, non-Darcy flow, surface diffusion, and stress dependence in organic-shale reservoirs. SPE J. 22 (1), 244–264. https://doi.org/10.2118/174996-PA.
Wang, L., Wang, S., Zhang, R., Wang, C., Xiong, Y., Zheng, X., Li, S., Jin, K., Rui, Z., 2017. Review of multi-scale and multi-physical simulation technologies for shale and tight gas reservoirs. J. Nat. Gas Sci. Eng. 37, 560–578. https://doi.org/10.1016/j.jngse.2016.11.051.
Wang, S., Feng, Q., Javadpour, F., Xia, T., 2015. Oil adsorption in shale nanopores and its effect on recoverable oil-in-place. Int. J. Coal Geol. 147, 9–24. https://doi.org/10.1016/j.coal.2015.06.002.
Wang, S., Shi, J., Wang, K., Sun, Z., Miao, Y., Hou, C., 2018. Apparent permeability model for gas transport in shale reservoirs with nano-scale porous media. J. Nat. Gas Sci. Eng. 55, 508–519. https://doi.org/10.1016/j.jngse.2018.05.026.
Wattenbarger, R.A., El-Banbi, A.H., Villegas, M.E., Maggard, J.B., 1998. Production analysis of linear flow into fractured tight gas wells. In: SPE Rocky Mountain Regional/Low-Permeability Reservoirs Symposium. https://doi.org/10.2118/39931-MS.
Wei, M., Duan, Y., Dong, M., Fang, Q., 2016. Blasingame decline type curves with material balance pseudo-time modified for multi-fractured horizontal wells in shale gas reservoirs. J. Nat. Gas Sci. Eng. 31, 340–350. https://doi.org/10.1016/j.jngse.2016.03.033.
Wu, J., Chang, Y.W., Liang, T., Guo, X.F., Chen, X.B., 2015. Seepage model of shale gas in matrix nanopores. Nat. Gas Geosci. 26 (3), 575–579. https://10.11764/j.issn.1672-1926.2015.03.0575.
Wu, K.L., Li, X.F., Chen, Z.X., 2015. The mechanism and mathematical model for the adsorbed gas surface diffusion in nanopores of shale gas reservoirs, 2015 Sci. Sin Tech. 45, 525–540 (in Chinese). https://10.1360/N092014-00263.
Wu, K.L., Chen, Z.X., Li, J., Li, X.F., Xu, J.Z., Dong, X.H., 2017. Wettability effect on nanoconfined water flow. Proc. Natl. Acad. Sci. U.S.A. 114 (13), 3358–3363. https://doi.org/10.1073/pnas.1612608114.
Yang, L., Mei, H., Zhang, M., 2016. Calculation method of shale gas reserves considering dissolved gas in kerogen. Xinjing Pet. Geol. 37 (5), 602–605. https://doi.org/10.7657/XJPG20160520 (in Chinese).
Yilmaz, Ö., Nolen-Hoeksema, R.C., Nur, A., 1994. Pore pressure profiles in fractured and compliant rocks1. Geophys. Prospect. 42 (6), 693–714. https://doi.org/10.1111/j.1365-2478.1994.tb00236.x.
Zeng, F., Zhang, Y., Guo, J., Ren, W., Jiang, Q., Xiang, J., 2020. Prediction of shale apparent liquid permeability based on fractal theory. Energy Fuel. 34 (6), 6822–6833. https://doi.org/10.1021/acs.energyfuels.0c00318.
Zhang, F., Emami-Meybodi, H., 2021a. Analysis of early-time production data from multi-fractured shale gas wells by considering multiple transport mechanisms through nanopores. J. Pet. Sci. Eng. 197, 108092. https://doi.org/10.1016/j.petrol.2020.108092.
Zhang, F., Emami-Meybodi, H., 2021b. Semianalytical method of two-phase liquid transport in shale reservoirs and its application in fracture characterization. AIChE J. 68 (2), e17449. https://doi.org/10.1002/aic.17449.
Zhang, F., Emami-Meybodi, H., 2022. A type-curve method for two-phase flowback analysis in hydraulically fractured hydrocarbon reservoirs. J. Pet. Sci. Eng. 209, 109912. https://doi.org/10.1016/j.petrol.2021.109912.
Zhang, L., Kang, Q.J., Yao, J., Gao, Y., Sun, H., 2014. The explanation of low recovery of fracturing fluid in shale hydraulic fracturing by pore-scale simulation. Chin. Sci. Bull. 59 (32), 3197–3203 (in Chinese). https://10.1360/N972014-00461.
Zhang, Q., Su, Y., Wang, W., Lu, M., Sheng, G., 2017. Apparent permeability for liquid transport in nanopores of shale reservoirs: coupling flow enhancement and near wall flow. Int. J. Heat Mass Tran. 115, 224–234. https://doi.org/10.1016/j.ijheatmasstransfer.2017.08.024.
Zhang, T., Li, X., Shi, J., Sun, Z., Yin, Y., Wu, K., Li, J., Feng, D., 2018. An apparent liquid permeability model of dual-wettability nanoporous media: a case study of shale. Chem. Eng. Sci. 187, 280–291. https://doi.org/10.1016/j.ces.2018.05.016.
Zhang, T., Li, X., Yin, Y., He, M., Liu, Q., Huang, L., Shi, J., 2019. The transport behaviors of oil in nanopores and nanoporous media of shale. Fuel 242, 305–315. https://doi.org/10.1016/j.fuel.2019.01.042.
Zhang, T., Javadpour, F., Li, X., Wu, K., Yin, Y., 2020. Mesoscopic method to study water flow in nanochannels with different wettability. Phys. Rev. E 102 (1), 013306. https://doi.org/10.1103/PhysRevE.102.013306.
Zhang, T., Javadpour, F., Li, J., Zhao, Y., Li, X., 2021. Pore-scale perspective of gas/water two-phase flow in shale. SPE J. 26 (2), 828–846. https://doi.org/10.2118/205019-PA.
Zhu, G.Y., Liu, L., Yang, Z.M., Liu, X.G., Cui, Y.T., 2007. Experiment and mathematical model of gas flow in low permeability porous media. In: Zhuang, F.G., Li, J.C. (Eds.), New Trends in Fluid Mechanics Research. Springer, Berlin, Heidelberg, pp. 534–537. https://doi.org/10.1007/978-3-540-75995-9_176.